

# BASED: Bundle-Adjusting Surgical Endoscopic Dynamic Video Reconstruction using Neural Radiance Fields

SHREYA SAHA<sup>1</sup>, ZEKAI LIANG<sup>1</sup>, SHAN LIN<sup>1</sup>, JINGPEI LU<sup>1</sup>, MICHAEL YIP<sup>1</sup> and SAINAN LIU<sup>2</sup>

<sup>1</sup>Electrical and Computer Engineering Dept., University of California San Diego, La Jolla, CA 92093, USA. (e-mail: ssaha, z9liang, shl102, jil360, yip@ucsd.edu)

<sup>2</sup>Intel Labs, USA. (e-mail: sainan.liu@intel.com)

Corresponding author: Zekai Liang (e-mail: z9liang@ucsd.edu).

**ABSTRACT** Reconstruction of deformable scenes from endoscopic videos is important for many applications such as intraoperative navigation, surgical visual perception, and robotic surgery. It is a foundational requirement for realizing autonomous robotic interventions for minimally invasive surgery. However, previous approaches in this domain have been limited by their modular nature and are confined to specific camera and scene settings. Our work adopts the Neural Radiance Fields (NeRF) approach to learning 3D implicit representations of scenes that are *both dynamic and deformable* over time, and furthermore with unknown camera poses. We demonstrate this approach on endoscopic surgical scenes from robotic surgery. This work removes the constraints of known camera poses and overcomes the drawbacks of the state-of-the-art unstructured dynamic scene reconstruction technique, which relies on the static part of the scene for accurate reconstruction. Through several experimental datasets, we demonstrate the versatility of our proposed model to adapt to diverse camera and scene settings, and show its promise for both current and future robotic surgical systems. Project Website: <https://sites.google.com/ucsd.edu/based-arclab-2023/>.

**INDEX TERMS** Endoscopic video, surgical scene reconstruction, bundle-adjusting reconstruction and pose estimation, implicit neural representation, deformable scene.

## I. INTRODUCTION

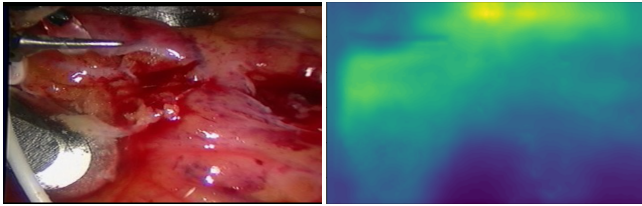
Surgical scene reconstruction from endoscopic videos is an important and challenging task in robotic-assisted minimally invasive surgery [1]. It also has widespread use in many downstream clinical applications such as surgical workflow analysis, image-guided robotic surgery, automation, surgical environment simulation, and augmented reality to train surgeons to be familiar with an operative environment and reconstruction of tissues and organs for preoperative assessment and planning. Many learning and automation algorithms for robotic surgery are reliant on accurate 3D reconstruction of the surgical scenes [2]–[4].

The majority of current approaches for reconstructing surgical scenes from endoscopic videos adopt a modular sequence of tasks, each tackled by independent models [5]–[13]. This fragmented methodology is susceptible to accumulating errors and lacks efficient task coordination. For instance, a significant number of existing methods either estimate or rely on ground truth camera poses before proceeding with scene reconstruction. Errors in pose estimation often lead to faulty scene reconstructions. Camera poses obtained through structure from motion (SfM) or simultaneous

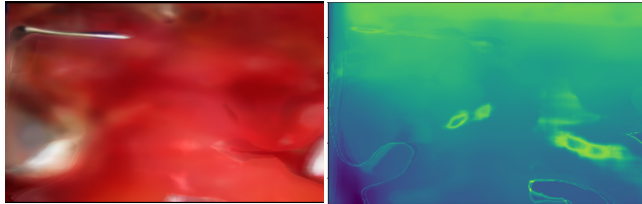
localization and mapping (SLAM) [14]–[18] often exhibit noise. When the camera is fixed to the end effector of a robotic arm, camera pose estimation can be accomplished through forward kinematics. However, these estimated poses are prone to errors stemming from inaccuracies in joint angle measurements attributed to instrument sag, cable stretch, positioning biases, and reading drift [19]. In reality, a further complication is that newer robotic systems are flexible, and these continuum robots (e.g., J&J Monarch Platform [20], Endomaster EASE System [21]) have complex mechanics that result in poor distal-camera localization. Furthermore, in addition to being modular, these methods will not generalize from static to deformable scene settings.

Neural Radiance Fields (NeRF) [22] has shown tremendous performance in the domain of 3D reconstruction. They have been applied recently to stereo-endoscopic videos for deformable surgery scene reconstruction [23], [24]. However, some constraints in these methods are that the camera should be static with stereo camera information and be in a known position. Alternatively, some works have extended NeRF with camera pose optimization (e.g., [25], [26]). However, these methods generally assume the scene to be static.

Ground Truth Color (left) and Depth (right)



RoDynRF (SOTA) color and depth



BASED (Ours) color and depth

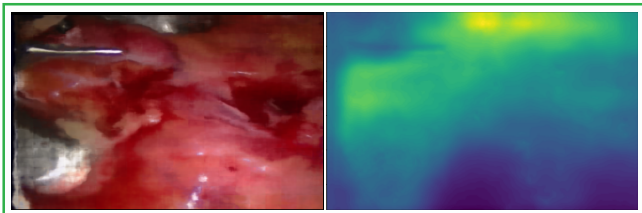


FIGURE 1: BASED is a novel NeRF-based method that can be used in dynamic and deformable scenes with unknown camera poses. It can produce novel viewpoint renderings with robust color (left) and depth (right) reconstructions, even from monocular untracked camera images. Comparisons with state-of-the-art methods (RoDynRF shown above, EndoNeRF failed completely) show that it has leading performance in scene reconstruction. Depth in the ground truth row is the reference depth, estimated from [6].

More recently, 3D Gaussian Splatting (3DGS) [27] was proposed as an alternative of NeRF. 3DGS represents the scene with a cloud of 3D Gaussians and estimate the Gaussian parameters based on a efficient rendering algorithm. Similar to NeRF, this technique has been applied to deformable surgical scenes with fixed or known camera poses [28], [29], as well as simultaneous estimation of static scene representations and unknown camera poses [30]. However, although 3DGS has achieved state-of-the-art visual rendering quality images, its scene representation – the 3D Gaussians – does not capture the 3D geometric information of the scene accurately enough. This is because surgical videos are typically highly under-constrained; that is, the camera movement is relatively small and the videos are captured from similar perspectives. Moreover, since training of 3DGS primarily focuses on minimizing the difference between rendered and actual images rather than learning accurate 3D geometry of the scene, Gaussians with realistic colors but inaccurate positions relative to the camera can still achieve good rendering results in under-constrained scenes. Thus, the geometric accuracy of the Gaussians, specifically their positions, highly depends on the quality of the point cloud and camera poses initialized using off-the-shelf SfM methods like COLMAP [31], [32], which still struggle to handle certain surgical videos. Therefore, we develop our method based on NeRF and demonstrate its improved ability

to capture scene geometry through several experiments.

In summary, we present the first NeRF-based method that can reconstruct deformable surgical scenes captured from untracked monocular endoscopic videos. The overall method combines a learnable pose layer that parameterizes camera poses, a deformation module that learns the deformation of a 3D point at a given time step with respect to a canonical position and a rendering module that takes the canonical coordinates of a 3D point at every time step along with the 2D camera directions and outputs the volumetric density and color information. We can solve for surgical scene representation learning, capturing more accurate geometric information without compromising on rendering capability for deforming scenes, even when the camera is a monocular camera, and in instances where the camera motion is unknown. This makes the method applicable to a wide range of robotic systems and semi-autonomous applications. The major contributions of this paper are thus:

- A NeRF approach for *dynamic and deformable* scenes from data captured at *unknown camera poses*,
- A method for describing multi-view correspondence loss, specifically catered to a dynamic and deformable setting, that enables establishing correspondence across spatiotemporal drift in tissues, and
- A framework that offers a generic, unrestricted, and versatile solution to robotic surgical perception that is validated on several surgical scene reconstruction datasets.

## II. RELATED WORK

### A. TRADITIONAL SCENE RECONSTRUCTION TECHNIQUES

Structure from Motion (SfM) utilizes a series of two-dimensional images to construct a three-dimensional model of a scene or an object, and it is widely used in the domain of scene/organ/tissue reconstruction with endoscopic images [8]–[13]. However, SfM techniques like COLMAP [31], [32] often fail to estimate camera poses for the entire length of sequences and often change the sequence of images. Simultaneous localization and mapping (SLAM) is a technique used to build a map of an unknown environment while simultaneously estimating the camera’s position and orientation in the environment. SLAM-based approaches [14]–[18] have been employed in the field of endoscopic scene reconstructions to model sparse and dense tissue surfaces. The scene is usually assumed to be static, and the estimated deformations do not always look natural.

### B. STATIC AND DYNAMIC NERF

NeRFs are implicit volumetric representations that encode the appearance and geometry of a 3D scene. It learns a continuous representation of the scene, enabling novel view renderings, unlike SLAM/SfM techniques that usually learn a discrete representation. It takes a 3D point coordinate and a 2D camera viewing direction and outputs RGB color information and the density of the point. The original NeRF model

strictly catered to static scenes. D-NeRF [33] is the first work that expanded the NeRF model to learn deformable scenes. It consists of two separate models that progressively learn the deformation and the volumetric scene reconstruction simultaneously. Robust Dynamic NeRF, or RoDynRF [34], tries to reconstruct dynamic scenes by estimating the camera poses using only the static part of the scene, which is not suitable for surgical scene reconstruction given that the scenes are highly deformable with a very low degree of rigidity. EndoNeRF [23] builds on D-NeRF for endoscopic scenes by adding a tool-guided ray casting and by sampling points along a ray closer to the tissue surfaces using a Gaussian transfer function but relying on stereo depth. EndoSurf [24] further improved upon EndoNeRF [23] by employing three networks to learn the deformation, signed distance function (SDF), and color of a viewpoint. However, as seen in Figure 1, these methods strictly cater to cases where the camera is static. If extended to moving camera sequences with camera poses estimated by COLMAP, the rendering quality degrades significantly.

### C. STATIC AND DYNAMIC GAUSSIAN SPLATTING

3DGS is a fast, learnable rendering technique for novel view synthesis. It uses 3D Gaussians for scene representation and a novel tile-based rasterizer for fast 3D Gaussian rendering. Given a set of camera poses and their corresponding 2D views, a cloud of 3D Gaussian representation (either randomly initialized or sparsely initialized via structure from motion point clouds) can be learned end-to-end. It yields state-of-the-art image quality as well as real-time inference speed. While the original work focused on static scenes, dynamic and deformable scenes have also been explored in recent months.

Dynamic 3D Gaussians [35] is the first to utilize 3D Gaussian splatting for multiview videos. It builds a static scene using 3DGS for the first frame, then incrementally learns the offset for each 3D Gaussian. However, the content is limited to the initial frame. Hence, it cannot model novel objects appearing in the middle of the video. More recent 3DGSream [36] has improved the efficiency of offset cache storage and enabled new Gaussian spawning. However, these models can only work with multiview images and rely heavily on the information from the first frame.

Yang *et al.* [37] and Wu *et al.* [38] both use a deformation field to model offsets to a canonical space of explicit 3D Gaussians, whereas [39] has increased GS dimension into 4D. However, these methods assume ground truth camera poses are known. Our model does not have this assumption.

### D. JOINT POSE ESTIMATION AND SCENE RECONSTRUCTION

Bundle adjusting neural radiance fields (BARF) [40] first proposed an end-to-end NeRF-based framework that can jointly estimate camera extrinsics and reconstruct the 3D scene. It implements a coarse-to-fine technique to gradually activate the higher frequency components of the positional encoding

scheme that aids in pose refinement, and only uses the photometric loss for backpropagation through the network. There have been numerous follow-up works ([25], [26], [41]–[47]) that improved BARF by optimizing its training time, adding prior losses and making it robust to in-the-wild sequences. More recently, similar ideas have also been explored with 3DGS [30], [48]. However, all of these methods specifically deal with static scenes. RoDynRF is a recent paper, to the best of our knowledge, that has first implemented estimating camera poses while simultaneously reconstructing dynamic scenes. They combine the pose estimation module from BARF with the radiance field module of Dynamic NeRF [49]. Although RoDynRF’s problem formulation is similar to ours, it cannot be easily adapted in surgical scene settings, requiring the dynamic pixels to be masked out prior to training, where a motion mask is generated using Mask R-CNN [50] and optical flow [51]. This is hard to acquire as the entire surgical scene may be deformable and textureless. Hence, as seen in Figure 1, it cannot be generalized for endoscopic videos. Our proposed model overcomes the limitations of EndoNeRF and EndoSurf by expanding to moving cameras with unknown poses. It does not constrain part of the scene to be static for it to be able to learn deformations, thus also overcoming the limitations of RoDynRF.

## III. METHODOLOGY

Figure 2 gives a high-level overview of our method. The overall model consists of three parts: (1) the pose estimation module (see III-A), (2) the deformable module (see III-B), and (3) a canonical NeRF module (see III-C).

### A. CAMERA POSE MODULE

We use a camera pose module to model the appearance of the rigid-body motion of the scene either caused by a moving camera or moving scene as is shown in Figure 2 (A). We follow the convention of previous work [40] and model the camera pose with  $P_i = [R_i | t_i] \in SE(3)$  representing camera-to-world transform of camera  $i$ , where  $R_i \in SO(3)$  denotes the rotation and  $t_i \in \mathbb{R}^3$  denotes the translation. We use  $K \in \mathbb{R}^{3 \times 3}$  to represent the intrinsic matrix.

In terms of implementation details, the poses are parameterized as a learnable parameter  $P_i \in \mathbb{R}^9$  for  $i \in [1, N]$  for  $N$  frames. The first six columns of the matrix refer to the first two rows of the camera rotation matrix, and the last three values refer to the camera translation vector. It should be noted that one can estimate the third row of the rotation matrix by taking a cross-product of the other two rows. The pose layer is initialized to identity and updated for the first 200 iterations, after which the layer is frozen.

### B. DEFORMATION MODULE

After the camera pose module explains away the rigid-body motion in the image, the deformation module will model the non-rigid-body deformation of the scene from a canonical state at  $t_0$  as is shown in Figure 2 (B). The deformation module  $\psi_\Delta(x, t)$  takes as input 3D spatial coordinates  $x \in \mathbb{R}^3$  and

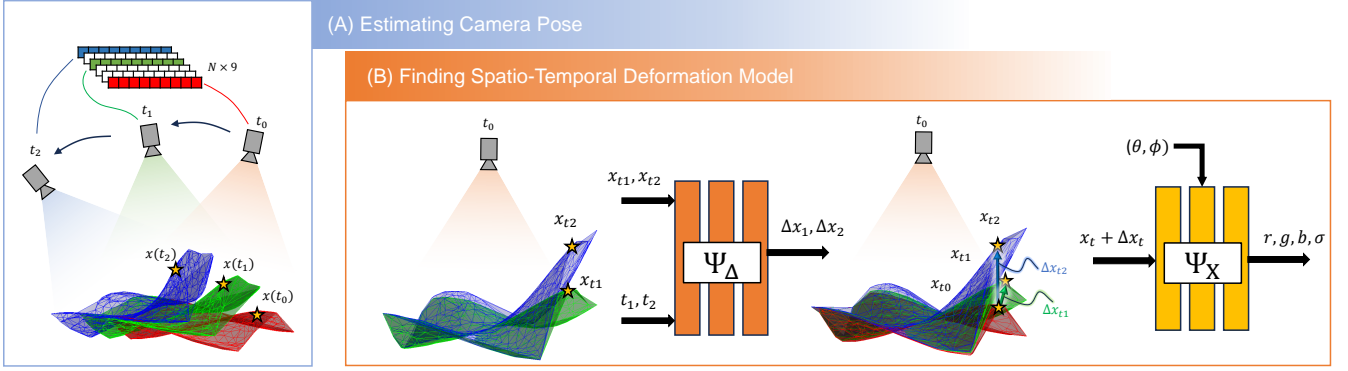


FIGURE 2: Method overview: (A) The first part of the diagram shows a tissue that appears to be dynamic and deformable at three timestamps  $t_0$ ,  $t_1$ , and  $t_2$ . Camera poses are estimated by a  $N \times 9$  learnable matrix through the camera pose estimation layer.  $x(t_0)$ ,  $x(t_1)$  and  $x(t_2)$  shows the trajectory taken by the same point  $x$  on the tissue at these three different timesteps. (B)  $x_{t_1}$  and  $x_{t_2}$  represents non-rigid deformation trajectory of  $x$  at time  $t_1$  and  $t_2$ . The deformation model denoted by  $\psi_\Delta$  takes in  $x_{t_1}$  and  $x_{t_2}$  and predicts their displacement from the canonical configuration of the scene. The canonical model  $\psi_x$  then takes in the mapped canonical position of the point  $x_{t_0} = x_{t_1} + \Delta x_{t_1} = x_{t_2} + \Delta x_{t_2}$  along with 2D camera directions, and predicts the color and density information.

a time step  $t$  and learns the deformation  $\Delta x$  of the coordinate  $x$  from time step zero:

$$\psi_\Delta(x, t) = \begin{cases} \Delta x & \text{if } t \neq 0 \\ 0 & \text{if } t = 0 \end{cases} \quad (1)$$

The idea is that the deformation can help us learn the position estimate of a point at the  $0^{th}$  time interval, which will be assumed the canonical configuration. If  $x_0$  is the coordinate of a point at time  $t = 0$  and it deforms to  $x_t$  at time  $t$ , then we can say that  $\psi_\Delta(x_t, t) + x_t = x_0$ .

### C. CANONICAL NERF MODULE

This module will capture the implicit 3D representation of the canonical state of the scene. The canonical module  $\psi_x$  can be assumed to be a vanilla NeRF model, which takes as input a spatial 3D location and 2D camera orientations, and outputs color (RGB values) and the volumetric density of the location.  $x_0$  calculated above is the input to the canonical model along with camera viewing directions  $d$ . The rendered output of the canonical model (color  $c$ , and density  $\sigma$ ) is corresponding to the deformed point  $x_t$  at time  $t$ .

$$\psi_x(x_t + \psi_\Delta(x_t, t), d) = c, \sigma \quad (2)$$

We apply conventional positional encoding [33] to all the inputs,  $\langle (\sin(2^l \pi p), \cos(2^l \pi p)) \rangle_0^L$ , with  $L = 10$  for 3D point coordinates  $x$  and time frame  $t$ , and  $L = 4$  for camera directions  $d$ . For more information about volumetric rendering, please refer to the original NeRF paper [22].

### D. TOOL MASK-GUIDED RAY CASTING AND STEREO DEPTH CUE RAY MARCHING

Surgical tools occlude part of the scene in most of our sequences. Instead of shooting rays randomly all through the image, we adopt a tool mask-guided ray casting strategy [23]. Using binary tool masks, an importance map is created which highlights the regions containing tool pixels. During training, instead of random ray sampling throughout the image, we only sample pixels from this distribution using inverse

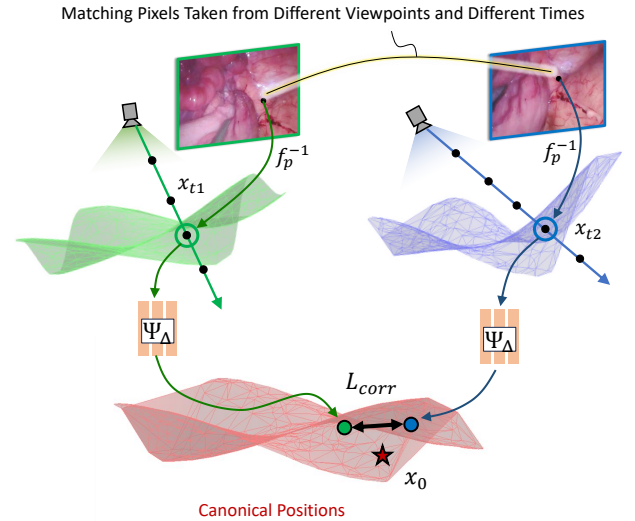


FIGURE 3: Overview of the correspondence loss: Matching pixels are chosen from a random pair of images (having correspondence above a certain threshold) using PDC-Net [52]. The matching pixels are projected from 2D pixel space to their 3D positions in the world frame, and then further passed through the deformation model to get their canonical 3D positions. The difference between the mapped 3D points is used to calculate the flow correspondence loss. The loss is designed to pull the outputs of correspondence points returned by the deformation model closer together towards the same canonical point denoted as  $x_0$ .

transform sampling. Secondly, we sample pixels close to the tissue surface using a Gaussian transfer function and use a depth refinement strategy to get rid of corrupt artifacts in the estimated depths.

### E. LOSSES

Our model uses photometric loss, correspondence loss, and estimated depth Loss for monocular dynamic camera deformable scene reconstruction.

**RGB Photometric Loss:** We use photometric loss based on conventional setup in NeRF models [22]. At every training iteration, we compare the rendered color of the sampled

pixels with the ground truth colors using the  $L_2$  loss, and this loss is backpropagated through the entire network with all three modules.

$$L_{pho} = \frac{1}{N} \sum_{i=1}^N \|\hat{C}_i(p, t) - C_i(p, t)\|_2^2 \quad (3)$$

where  $\hat{C}_i$  is the rendered color and  $C_i$  is the ground truth color of the pixel  $p$  at time  $t$  with respect to frame  $i$ ,  $i = 0 \dots N$ .

**Dynamic Multi-View Correspondence Loss:** We introduce a novel 3D multi-view correspondence loss for dynamic scenes to offer extra constraints on pose estimation. Figure 3 gives a high-level idea of this loss. For a given pair of images,  $I_i^a$  (viewpoint  $P_i$  at time  $t_a$ ) and  $I_j^b$  (viewpoint  $P_j$  at time  $t_b$ ) with matching pixels  $p^a \in I_i^a$  and  $q^b \in I_j^b$ , both pixels  $p^a$  and  $q^b$  should project to the same point in 3D space in the canonical space.  $z_p^a$  and  $z_q^b$  are the estimated depths of the pixels  $p^a$  and  $q^b$  respectively. Let  $f_{P_i}^{-1}$  be the function that maps the 3D coordinate of a pixel given its estimated depth and its respective camera viewpoint. Let  $x_p^a \in \mathbb{R}^3$  be the 3D coordinate of pixel  $p^a$  at time  $t_a$  and  $x_q^b \in \mathbb{R}^3$  be the 3D coordinate of pixel  $q^b$  at time  $t_b$ . Then, the estimated coordinates are

$$x_p^a = f_{P_i}^{-1}(p^a, z_p^a) \quad (4)$$

$$x_q^b = f_{P_j}^{-1}(q^b, z_q^b) \quad (5)$$

If there was no deformation,  $x_p^a$  and  $x_q^b$  should be the same point in 3D space. However, since this is a deformable scene, we need to map both the points back to their canonical state in order to calculate the loss:

$$\hat{x}_p^a = \psi_{\Delta}(x_p^a, t_a) + x_p^a \quad (6)$$

$$\hat{x}_q^b = \psi_{\Delta}(x_q^b, t_b) + x_q^b \quad (7)$$

Then, the loss becomes:

$$L_{corr} = w(L_{\delta}(\hat{x}_p^a, \hat{x}_q^b)) \quad (8)$$

where  $w$  is loss weight term and  $L_{\delta}$  is the Huber loss function.

**Estimated Depth Loss:** In spite of only having 2D images, we can use an *estimated* depth loss to further assist better reconstruction when the camera pose estimation is optimized. The depth estimates can be found via an off-the-shelf image-to-depth estimator. This loss is only used to optimize the deformable and canonical modules after the pose layer is frozen. Applying the estimated depth loss before the camera pose matrix is optimized leads to abrupt artifacts. We collect depths estimated from RGB images via existing pre-trained methods [53], [6] during training. We compare the rendered depth values of the sampled pixels with the corresponding estimated depth values using a  $L_2$  loss. The gradient from this loss is only backpropagated through the deformable NerRF modules, after the pose layer is frozen.

$$L_d = \frac{1}{N} \sum_{i=1}^N \|\hat{D}_i(p, t) - D_i(p, t)\|_2^2 \quad (9)$$

where  $\hat{D}_i(p, t) = \frac{1}{\sigma_i(p, t)}$  is the rendered depth,  $\sigma_i$  is the rendered density and  $D_i(p, t)$  is the reference depth of the pixel  $p$  at time  $t$  with respect to frame  $i \in [1, N]$  for  $N$  frames. Note that if a hardware solution to depth is available (e.g., stereo cameras or RGB-D sensor, the ground truth depth can be used as well to calculate an estimated depth loss.

## IV. EXPERIMENTS

### A. IMPLEMENTATION DETAILS

All of the experiments have been performed on a single Nvidia RTX-A6000 GPU. The weights of the NeRF network and the pose estimation network are simultaneously updated with a learning rate of 5e-4. After 200 iterations, the pose layer is fixed, and only the NeRF model is updated for another 100K iterations. In the first stage, one batch consists of all of the training images, because it requires more views of the scene for better pose estimation. In the second stage, one batch consists of a single training image for faster training. Tool masks are manually created for the Hamlyn dataset sequences, partly using Segment Anything Model [54]. We use an off-the-shelf dense pixel correspondence network, PDC-Net [55], to obtain corresponding matching pixels between a pair of images for calculating the multi-view correspondence loss  $L_{corr}$ .

### B. DATASETS

We evaluated BASED on the following datasets:

**Hamlyn Dataset** [56]: We choose three videos from the Hamlyn dataset of robotic surgery with deformable scenes. Hamlyn dataset contains weak textures, and the scene is often occluded by blood and surgical instruments. Rectified04 contains 158 frames, and it appears to have slight camera motion. The camera in Rectified04 is mostly static, whereas Rectified18 exhibits slightly more camera motion, so two subsets of Rectified18 are chosen from the whole video with 113 frames in each. The frames are sampled at regular intervals (every 10 frames), as the original videos were too large. 10 percent of the total images were used for testing. We use [6] to generate reference depth needed for calculating the estimated depth loss.

**EndoNeRF da Vinci dataset** [23]: We used only two datasets used in the EndoNeRF paper that are publicly available. They last for 4-8 sec with 15 fps. Each of the videos is taken from a single static viewpoint setting. One of the videos demonstrates soft tissues being drastically pulled in 2 seconds, while the other video demonstrates soft tissue cutting with challenging topological changes. As mentioned in the original paper, the depth maps are obtained using STTR-LIGHT [53] from stereo images. The train-test split is the same as it is used in the original paper.

### C. METRICS

The quality of image rendering is evaluated through commonly used metrics, including (1) Peak Signal-to-Noise

TABLE 1: Ablation studies on Hamlyn Rectified18-1 dataset with dynamic motions.

	BA	$L_d$	$L_{corr}$	PSNR $\uparrow$	SSIM $\uparrow$	LPIPS $\downarrow$
EndoNeRF [23]	COLMAP	✓	-	26.97	0.895	0.164
BASED w/o $L_d L_{corr}$	✓	-	-	30.236	0.925	0.124
BASED w/o $L_d$	✓	-	✓	31.415	0.935	0.108
BASED w/o $L_{corr}$	✓	✓	-	31.403	0.937	<b>0.102</b>
BASED (final)	✓	✓	✓	<b>32.227</b>	<b>0.944</b>	0.106

✓ indicates loss usage.

BA stands for bundle-adjusting.

EndoNeRF experiment is using COLMAP for camera pose estimation.

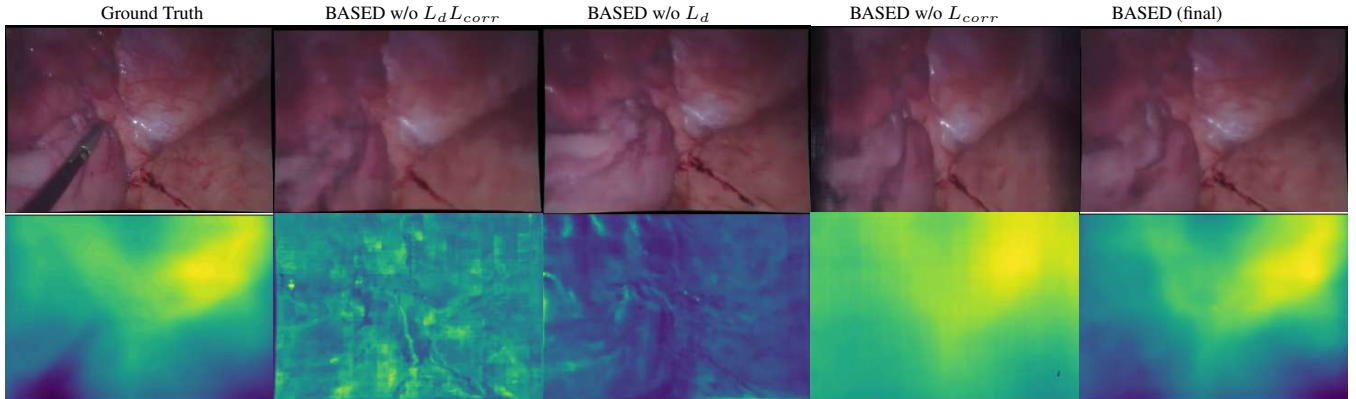


FIGURE 4: Ablation analysis on Hamlyn Rectified 18-1 dataset shows how different losses bring about an improvement in the rendered results from the final model. Please note that the depth in the Ground Truth column is the reference depth.

Ratio (PSNR), (2) Learned Perceptual Image Patch Similarity (LPIPS) [57], and (3) Structural Similarity Index (SSIM) [57]. We also quantitatively evaluate the 3D reconstruction performance by comparing predicted depth maps with the reference depth (refer to Section IV-B for details), using standard metrics for depth evaluation [58]. With this, we are treating the reference as pseudo ground truth. It should be noted that while the quality this pseudo ground truth may be slightly inferior than that of true depth, using it is still a common strategy in endoscopic video analysis as true ground truth can be hard to obtain in a surgical environment [59].

## D. RESULTS

### 1) Ablation Study

Table 1 and Figure 4 provide both quantitative and qualitative analysis of the effect of the various losses on the performance of our model. As shown in Table 1, bundle-adjusting leads to significant improvement in image rendering quality compared with EndoNeRF [23], a state-of-the-art NeRF-based model developed for a similar task. Also, training with estimated depth guidance  $L_d$  and correspondence loss  $L_{corr}$  improves rendering quality, respectively. Figure 4 shows that estimated depth guidance clearly improves the reconstructed textures and depths. Additionally, correspondence loss  $L_{corr}$  leads to better results, as shown quantitatively by image rendering results and qualitatively by predicted depth quality, indicating that the correspondence loss may have improved the estimated camera poses by instilling multi-view consistency in this dynamic deformable scene, which in turn

leads to better convergence of the deformable NeRF model. However, the sequences are still severely underconstrained (camera movement/viewing angles of the scene are still limited in those sequences, which is common in surgical scenes), hence the correspondence loss only showed a relatively slight improvement in depth reconstruction. The tool masks for sequence - Rectified04-1 from the Hamlyn dataset does not always completely mask out the tools, which is why the resultant rendered images partially have tools in them (Figure 1), and not a transparent overlay like we see for the other rendered results.

### 2) Comparison on Hamlyn Dataset

The main dataset we are evaluating is the Hamlyn dataset. We compare BASED with state-of-the-art methods including EndoNeRF, RoDynRF and EndoGS, for deformable scene reconstruction with obvious camera motions. The image rendering quality are quantitatively and qualitatively compared in Table 2 and Figure 6, respectively. The 3D scene reconstruction performance is evaluated through depth maps predicted by the models, which are also provided in Figure 6. Our model outperforms both EndoNeRF and RoDynRF by a significant margin in both image rendering and 3D reconstruction.

On the other hand, BASED is still competitive in image rendering compared with EndoGS, which is based on 3DGS. 3DGS has inherent advantages in image rendering, as the color and position of the Gaussians can be easily updated to fit the camera view. However, the Gaussian cloud es-

TABLE 2: Quantitative analysis of BASED and State-of-the-Art on the Hamlyn Dataset.

	PSNR $\uparrow$				SSIM $\uparrow$				LPIPS $\downarrow$			
	EndoNeRF	RoDynRF	EndoGS	Ours	EndoNeRF	RoDynRF	EndoGS	Ours	EndoNeRF	RoDynRF	EndoGS	Ours
Rectified04-1 (scds)	-	<u>14.902</u>	-	<b>20.947</b>	-	0.468	-	<b>0.621</b>	-	<u>0.577</u>	-	<b>0.269</b>
Rectified18-1 (mcds)	22.838	25.700	<u>30.821</u>	<b>32.277</b>	0.817	0.874	<u>0.928</u>	<b>0.944</b>	0.273	0.192	<b>0.100</b>	<u>0.106</u>
Rectified18-2 (mcds)	29.572	24.690	<b>35.969</b>	<u>33.017</u>	0.869	0.875	<b>0.956</b>	<u>0.936</u>	0.235	0.201	<b>0.079</b>	<u>0.103</u>

'-' denotes that the model fails to complete the task.  
 Best results are **bolded**; second best are underlined.

TABLE 3: Quantitative analysis of BASED and EndoGS depth estimation on the Hamlyn Rectified18-2 dataset.

	Abs Rel $\downarrow$	Sq Rel $\downarrow$	RMSE $\downarrow$	RMSE Log $\downarrow$	$\delta < 1.25 \uparrow$	$\delta < 1.25^2 \uparrow$	$\delta < 1.25^3 \uparrow$
EndoGS	3.834	1.149	2.938	4.225	3.356	6.908	10.930
BASED	<b>1.124</b>	<b>0.228</b>	<b>1.790</b>	<b>1.341</b>	<b>10.227</b>	<b>11.000</b>	<b>11.000</b>

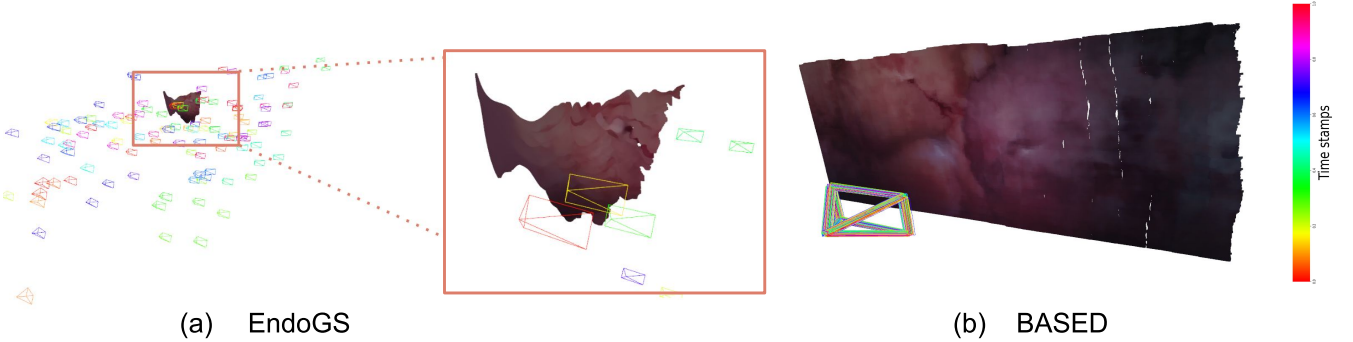


FIGURE 5: Camera poses and point cloud visualization of (a) EndoGS and (b) BASED on hamlyn dataset Rectified18-2. The colors assigned to the cameras correspond to their timestamps in the video.

TABLE 4: Quantitative analysis of BASED and state-of-the-art on the EndoNeRF da Vinci dataset.

	PSNR $\uparrow$				SSIM $\uparrow$				LPIPS $\downarrow$			
	EndoNeRF	RoDynRF	EndoGS	Ours	EndoNeRF	RoDynRF	EndoGS	Ours	EndoNeRF	RoDynRF	EndoGS	Ours
pulling soft tissues	<u>35.832</u>	27.502	<b>36.750</b>	35.097	<b>0.941</b>	0.900	0.925	<u>0.936</u>	<b>0.058</b>	0.158	0.135	<u>0.059</u>
cutting tissues twice	<u>35.720</u>	21.105	<b>37.372</b>	35.706	<u>0.935</u>	0.700	<b>0.964</b>	0.934	<u>0.063</u>	0.280	<b>0.050</b>	0.073

Best results are **bolded**; second best are underlined.

timated by EndoGS may not accurately represent the true geometric shape of the environment, which is critical for many downstream tasks in surgical applications. To demonstrate the superiority of our method in capturing the 3D geometric information of the scene, beyond Figure 6, we also quantitatively measure the quality of predicted depth based on the reference depth, as shown in Table 3. BASED provides better depth maps than EndoGS both quantitatively and qualitatively. Furthermore, we visualize the camera pose along with the point cloud estimated by EndoGS and BASED in Figure 5. Given the small camera motion in this dataset, the true camera poses are expected to be close over time. BASED aligns more closely with this pattern compared to EndoGS. A major drawback of EndoNeRF and EndoGS is that they have only been tested on video sequences with single-view static cameras, which are severely under-constrained. To apply EndoNeRF and EndoGS to dynamic scenes, both models use COLMAP to estimate camera poses. Thus, these two models

fail when COLMAP fails to predict camera poses as seen for Rectified 04-1 in Table 2. This clearly demonstrates the superiority of our method. Also, even in cases where COLMAP is able to estimate camera poses, our model, BASED, more accurately captures the dynamic and deformable aspects of the scene, as shown by the quantitative and qualitative results provided.

### 3) Comparison on EndoNeRF da Vinci Dataset

We further show that our model can generalize toward deformable surgical scenes with stationary cameras on the sequences used in the EndoNeRF paper: Cutting tissues twice and Pulling soft tissues. Table 4 and Figure 7 show a quantitative and qualitative evaluation of the performance of our model versus baseline EndoNeRF, RoDynRF. We can see that our model is on par, if not better than EndoNeRF, and performs significantly better than RoDynRF. In Figure 8, our model is able to generalize better to novel view renderings

TABLE 5: Quantitative analysis of BASED and EndoGS depth estimation on the EndoNeRF "Cutting Tissues Twice" dataset.

	Abs Rel↓	Sq Rel↓	RMSE↓	RMSE Log↓	$\delta < 1.25 \uparrow$	$\delta < 1.25^2 \uparrow$	$\delta < 1.25^3 \uparrow$
EndoGS	$4.644 \times 10^6$	$1.643 \times 10^6$	<b>54.342</b>	622.943	52.230	69.472	85.756
BASED	<b>47.931</b>	<b>27.107</b>	65.810	<b>140.360</b>	<b>91.750</b>	<b>92.898</b>	<b>93.772</b>

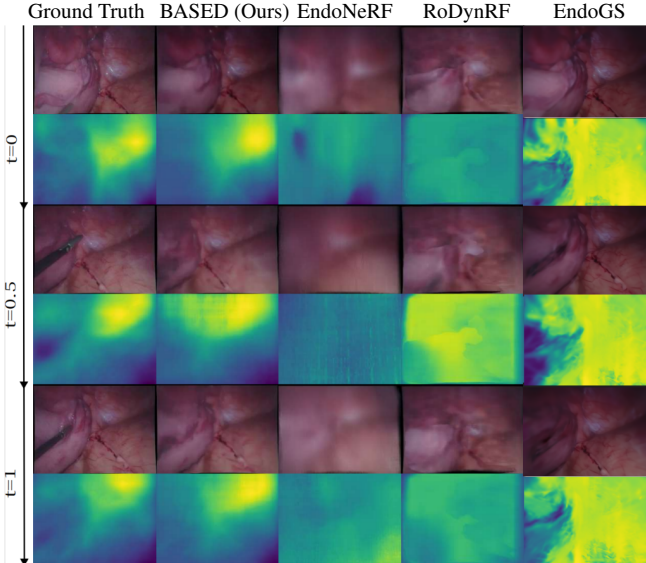


FIGURE 6: Qualitative analysis of our proposed model BASED compared with RoDynRF, EndoNeRF and EndoGS (with COLMAP estimated poses) for sequences obtained from the public Hamlyn dataset. Please note that the depth in the Ground Truth column is the reference depth.

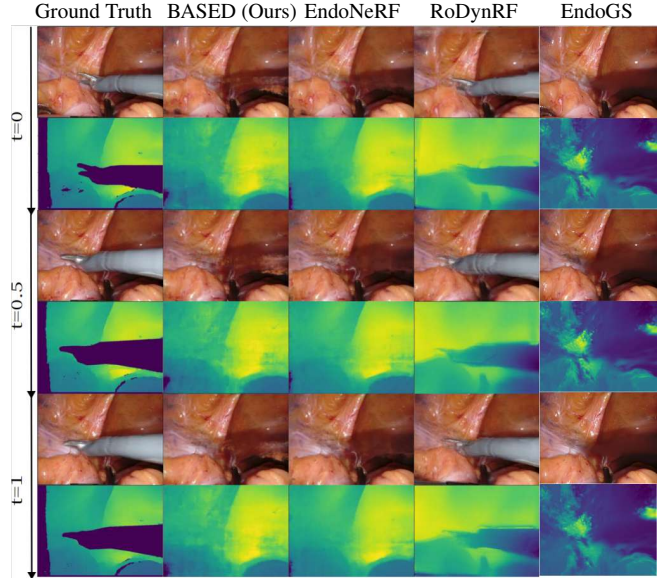


FIGURE 7: Qualitative analysis of our proposed model BASED with RoDynRF and EndoNeRF for two publicly available sequences - "Cutting Tissues Twice" [23] guided by stereo depth.

compared to EndoNeRF which has been strictly trained with static identity camera poses. Hence, our model retains EndoNeRF's capacity for static deformable monocular videos.

Furthermore, we still compare our model with EndoGS on static surgical scenes. From Table 5 and Figure 7, both qualitative and quantitative results show although EndoGS shows its inherent advantage in image rendering, it still almost fails in geometric shape capturing even on static camera scenes, which is very crucial for real-world applications of 3D scene reconstruction.

## V. CONCLUSION

We propose BASED, a network that simultaneously estimates dynamic scene motions and reconstructs deformable surgical scenes from monocular videos. To the best of our knowledge, this is the first work that tries to reconstruct scenes from video sequences where the static and the dynamic parts cannot be clearly differentiated from one another, and also the first work that attempts to reconstruct deformable surgical scenes with unknown camera poses from monocular videos. Through our experiments, we have shown significant improvement over the existing state-of-the-art methods in this domain, and also potential for future research. Limitations of the presented model include slow optimization time (similar to EndoNeRF at several hours), though many recent strategies are drastically cutting this time by orders

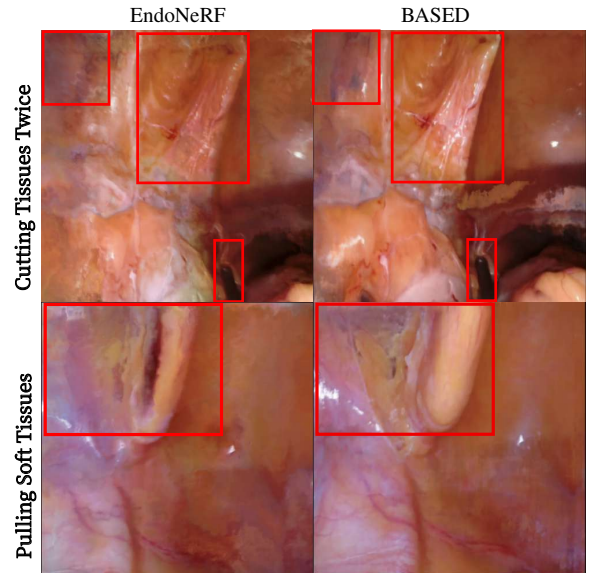


FIGURE 8: Qualitative analysis of our proposed model BASED and EndoNeRF on "Cutting Tissues Twice" dataset for novel view renderings. Highlighted sections show how BASED is able to avoid different artifacts in the images, resulting in a sharper image.

of magnitude (including ours [26]). Some potential future directions could be removing the dependency of BASED on reference depths, reducing optimization time, and automatic tool mask generation.

## REFERENCES

- [1] M. Yip, S. Salcudean, K. Goldberg, K. Althoefer, A. Mencias, J. D. Opfermann, A. Krieger, K. Swaminathan, C. J. Walsh, H. Huang, et al., "Artificial intelligence meets medical robotics," *Science*, vol. 381, no. 6654, pp. 141–146, 2023.
- [2] F. Liu, Z. Li, Y. Han, J. Lu, F. Richter, and M. C. Yip, "Real-to-sim registration of deformable soft tissue with position-based dynamics for surgical robot autonomy," in *IEEE Int. Conf. Robot. Autom.*, pp. 12328–12334, IEEE, 2021.
- [3] X. Liang, F. Liu, Y. Zhang, Y. Li, S. Lin, and M. Yip, "Real-to-sim deformable object manipulation: Optimizing physics models with residual mappings for robotic surgery," arXiv preprint arXiv:2309.11656, 2023.
- [4] N. U. Shinde, X. Liang, F. Liu, Y. Zhang, F. Richter, S. Herbert, and M. C. Yip, "Jiggle: An active sensing framework for boundary parameters estimation in deformable surgical environments," arXiv preprint arXiv:2405.09743, 2024.
- [5] Y. Long, Z. Li, C. H. Yee, C. F. Ng, R. H. Taylor, M. Unberath, and Q. Dou, "E-DSSR: Efficient dynamic surgical scene reconstruction with transformer-based stereoscopic depth perception," in *Medical Image Computing and Computer Assisted Intervention—MICCAI 2021: 24th International Conference, Strasbourg, France, September 27–October 1, 2021, Proceedings, Part IV 24*, pp. 415–425, Springer, 2021.
- [6] D. Recasens, J. Lamarca, J. M. Fácil, J. Montiel, and J. Civera, "Endo-depth-and-motion: Reconstruction and tracking in endoscopic videos using depth networks and photometric constraints," *IEEE Int. Conf. Robot. Autom. Letters*, vol. 6, no. 4, pp. 7225–7232, 2021.
- [7] Z. Li, X. Liu, N. Drenkow, A. Ding, F. X. Creighton, R. H. Taylor, and M. Unberath, "Revisiting stereo depth estimation from a sequence-to-sequence perspective with transformers," in *Int. Conf. Comput. Vis.*, pp. 6197–6206, October 2021.
- [8] K. L. Lurie, R. Angst, D. V. Zlatev, J. C. Liao, and A. K. Ellerbee Bowden, "3D reconstruction of cystoscopy videos for comprehensive bladder records," *Biomed. Opt. Expr.*, pp. 2106–2123, 2017.
- [9] T. D. Soper, M. P. Porter, and E. J. Seibel, "Surface mosaics of the bladder reconstructed from endoscopic video for automated surveillance," *IEEE Trans. Biomed. Eng.*, pp. 1670–1680, 2012.
- [10] M. Hu, G. Penney, M. Figl, P. Edwards, F. Bello, R. Casula, D. Rueckert, and D. Hawkes, "Reconstruction of a 3D surface from video that is robust to missing data and outliers: Application to minimally invasive surgery using stereo and mono endoscopes," *Med. Image Anal.*, 2012.
- [11] A. R. Widya, Y. Monno, K. Imahori, M. Okutomi, S. Suzuki, T. Gotoda, and K. Miki, "3d reconstruction of whole stomach from endoscope video using structure-from-motion," in *Proc. 41st Annu. Int. Conf. IEEE Eng. Med. Biol. Soc.*, 2019, pp. 3900–3904.
- [12] T.-B. Phan, D.-H. Trinh, D. Wolf, and C. Daul, "Optical flow-based structure-from-motion for the reconstruction of epithelial surfaces," *Pattern Recognition*, vol. 105, p. 107391, 2020.
- [13] A. R. Widya, Y. Monno, M. Okutomi, S. Suzuki, T. Gotoda, and K. Miki, "Whole stomach 3D reconstruction and frame localization from monocular endoscope video," *IEEE J. Transl. Eng. Health Med.*, vol. 7, pp. 1–10, 2019.
- [14] J. Lamarca, S. Parashar, A. Bartoli, and J. M. M. Montiel, "DefSLAM: Tracking and mapping of deforming scenes from monocular sequences," *IEEE Trans. Robot.*, vol. 37, pp. 291–303, February 2021.
- [15] J. J. G. Rodríguez, J. Lamarca, J. Morlana, J. D. Tardós, and J. M. Montiel, "SD-DefSLAM: Semi-direct monocular slam for deformable and intracorporeal scenes," in *IEEE Int. Conf. Robot. Autom.*, pp. 5170–5177, 2021.
- [16] J. Song, J. Wang, L. Zhao, S. Huang, and G. Dissanayake, "MIS-SLAM: Real-time large scale dense deformable slam system in minimal invasive surgery based on heterogeneous computing," *IEEE Int. Conf. Robot. Autom. Letters*, vol. PP, pp. 4068–4075, 03 2018.
- [17] O. García-Grasa, E. Bernal, S. Casado, I. Gil, and J. Montiel, "Visual SLAM for handheld monocular endoscope," *IEEE Trans. Med. Imag.*, vol. 33, pp. 135–146, 09 2013.
- [18] X. Liu, Z. Li, M. Ishii, G. D. Hager, R. H. Taylor, and M. Unberath, "SAGE: SLAM with appearance and geometry prior for endoscopy," in *IEEE Int. Conf. Robot. Autom.*, pp. 5587–5593, 2022.
- [19] F. Richter, J. Lu, R. K. Orosco, and M. C. Yip, "Robotic tool tracking under partially visible kinematic chain: A unified approach," *IEEE Trans. Robot.*, vol. 38, no. 3, pp. 1653–1670, 2021.
- [20] "Auris health inc, johnson and johnson, monarch platform," <https://www.jnjmedtech.com/en-us/product-family/monarch/>, 2018.
- [21] "Endomaster pte ltd, endomaster ease system," <http://www.endomastermedical.com/>, 2018.
- [22] B. Mildenhall, P. P. Srinivasan, M. Tancik, J. T. Barron, R. Ramamoorthi, and R. Ng, "NeRF: Representing scenes as neural radiance fields for view synthesis," in *Eur. Conf. Comput. Vis.*, 2020.
- [23] Y. Wang, Y. Long, S. H. Fan, and Q. Dou, "Neural rendering for stereo 3D reconstruction of deformable tissues in robotic surgery," in *Med. Imag. Comput. Comput. Assis. Interv.*, pp. 431–441, Springer, 2022.
- [24] R. Zha, X. Cheng, H. Li, M. Harandi, and Z. Ge, "Endosurf: Neural surface reconstruction of deformable tissues with stereo endoscope videos," in *Med. Imag. Comput. Comput. Assis. Interv.*, pp. 13–23, Springer, 2023.
- [25] Y. Chen and G. H. Lee, "DBARF: Deep bundle-adjusting generalizable neural radiance fields," in *IEEE Conf. Comput. Vis. Pattern Recog.*, pp. 24–34, June 2023.
- [26] S. Liu, S. Lin, J. Lu, S. Saha, A. Supikov, and M. Yip, "BAA-NGP: Bundle-adjusting accelerated neural graphics primitives," arXiv, 2023.
- [27] B. Kerbl, G. Kopanas, T. Leimkühler, and G. Drettakis, "3D gaussian splatting for real-time radiance field rendering," *ACM Trans. Graph.*, vol. 42, no. 4, pp. 1–14, 2023.
- [28] L. Zhu, Z. Wang, J. Cui, Z. Jin, G. Lin, and L. Yu, "EndoGS: Deformable endoscopic tissues reconstruction with gaussian splatting,"
- [29] Y. Liu, C. Li, C. Yang, and Y. Yuan, "EndoGaussian: Gaussian splatting for deformable surgical scene reconstruction," arXiv preprint arXiv:2401.12561, 2024.
- [30] Y. Fu, S. Liu, A. Kulkarni, J. Kautz, A. A. Efros, and X. Wang, "COLMAP-Free 3D gaussian splatting," arXiv preprint arXiv:2312.07504, 2023.
- [31] J. L. Schönberger and J.-M. Frahm, "Structure-from-motion revisited," in *IEEE Conf. Comput. Vis. Pattern Recog.*, 2016.
- [32] J. L. Schönberger, E. Zheng, M. Pollefeys, and J.-M. Frahm, "Pixelwise view selection for unstructured multi-view stereo," in *Proc. European Conf. Comput. Vis.*, 2016.
- [33] A. Pumarola, E. Corona, G. Pons-Moll, and F. Moreno-Noguer, "D-NeRF: Neural radiance fields for dynamic scenes," in *IEEE Conf. Comput. Vis. Pattern Recog.*, pp. 10318–10327, 2021.
- [34] Y.-L. Liu, C. Gao, A. Meuleman, H.-Y. Tseng, A. Saraf, C. Kim, Y.-Y. Chuang, J. Kopf, and J.-B. Huang, "Robust dynamic radiance fields," in *IEEE Conf. Comput. Vis. Pattern Recog.*, 2023.
- [35] J. Luiten, G. Kopanas, B. Leibe, and D. Ramanan, "Dynamic 3D Gaussians: Tracking by persistent dynamic view synthesis," in *3DV*, 2024.
- [36] J. Sun, H. Jiao, G. Li, Z. Zhang, L. Zhao, and W. Xing, "3DGStream: On-the-fly training of 3D gaussians for efficient streaming of photo-realistic free-viewpoint videos," arXiv preprint arXiv:2403.01444, 2024.
- [37] Z. Yang, X. Gao, W. Zhou, S. Jiao, Y. Zhang, and X. Jin, "Deformable 3D Gaussians for high-fidelity monocular dynamic scene reconstruction," arXiv preprint arXiv:2309.13101, 2023.
- [38] G. Wu, T. Yi, J. Fang, L. Xie, X. Zhang, W. Wei, W. Liu, Q. Tian, and X. Wang, "4D gaussian splatting for real-time dynamic scene rendering," arXiv preprint arXiv:2310.08528, 2023.
- [39] Z. Yang, H. Yang, Z. Pan, and L. Zhang, "Real-time photorealistic dynamic scene representation and rendering with 4D gaussian splatting," in *Int. Conf. Learn. Represent.*, 2024.
- [40] C.-H. Lin, W.-C. Ma, A. Torralba, and S. Lucey, "BARF: Bundle-adjusting neural radiance fields," in *Int. Conf. Comput. Vis.*, 2021.
- [41] Y. Jeong, S. Ahn, C. Choy, A. Anandkumar, M. Cho, and J. Park, "Self-calibrating neural radiance fields," in *Int. Conf. Comput. Vis.*, 2021.
- [42] P. Truong, M.-J. Rakotosaona, F. Manhardt, and F. Tombari, "SPARF: Neural radiance fields from sparse and noisy poses," in *IEEE Conf. Comput. Vis. Pattern Recog.*, 2023.
- [43] S.-F. Chng, S. Ramasinghe, J. Sherrah, and S. Lucey, "Gaussian activated neural radiance fields for high fidelity reconstruction and pose estimation," in *Eur. Conf. Comput. Vis.*, 2022.
- [44] Z. Cheng, C. Esteves, V. Jampani, A. Kar, S. Maji, and A. Makadia, "LU-NeRF: Scene and pose estimation by synchronizing local unposed NeRFs," 2023.
- [45] Y. Xia, H. Tang, R. Timofte, and L. V. Gool, "SiNeRF: Sinusoidal neural radiance fields for joint pose estimation and scene reconstruction," in *Proc. 33rd Brit. Mach. Vis. Conf.*, London, UK, Nov. 21–24, 2022.
- [46] W. Bian, Z. Wang, K. Li, J.-W. Bian, and V. A. Prisacariu, "NoPe-NeRF: Optimising neural radiance field with no pose prior," in *Proc. IEEE/CVF Conf. Comput. Vis. Pattern Recog.*, pp. 4160–4169, 2023.
- [47] A. Meuleman, Y.-L. Liu, C. Gao, J.-B. Huang, C. Kim, M. H. Kim, and J. Kopf, "Progressively optimized local radiance fields for robust view synthesis," in *IEEE Conf. Comput. Vis. Pattern Recog.*, 2023.

- [48] L. Zhao, P. Wang, and P. Liu, "BAD-Gaussians: Bundle adjusted deblur gaussian splatting," arXiv preprint arXiv:2403.11831, 2024.
- [49] C. Gao, A. Saraf, J. Kopf, and J.-B. Huang, "Dynamic view synthesis from dynamic monocular video," in *Int. Conf. Comput. Vis.*, 2021.
- [50] W. Abdulla, "Mask R-CNN for object detection and instance segmentation on Keras and TensorFlow," 2017.
- [51] Z. Teed and J. Deng, "Raft: Recurrent all-pairs field transforms for optical flow," in *Eur. Conf. Comput. Vis.*, 2020.
- [52] P. Truong, M. Danelljan, L. Van Gool, and R. Timofte, "Learning accurate dense correspondences and when to trust them," in *Proc. IEEE/CVF Conf. Comput. Vis. Pattern Recognit.*, pp. 5714–5724, 2021.
- [53] Z. Li, X. Liu, N. Drenkow, A. Ding, F. X. Creighton, R. H. Taylor, and M. Unberath, "Revisiting stereo depth estimation from a sequence-to-sequence perspective with transformers," in *Proceedings of the IEEE/CVF international conference on computer vision*, pp. 6197–6206, 2021.
- [54] A. Kirillov, E. Mintun, N. Ravi, H. Mao, C. Rolland, L. Gustafson, T. Xiao, S. Whitehead, A. C. Berg, W.-Y. Lo, P. Dollár, and R. Girshick, "Segment anything," arXiv, 2023.
- [55] P. Truong, M. Danelljan, L. Van Gool, and R. Timofte, "Learning accurate dense correspondences and when to trust them," in *Proc. IEEE/CVF Conf. Comput. Vis. Pattern Recognit.*, pp. 5714–5724, 2021.
- [56] M. Ye, E. Johns, A. Handa, L. Zhang, P. Pratt, and G.-Z. Yang, "Self-supervised siamese learning on stereo image pairs for depth estimation in robotic surgery," arXiv preprint arXiv:1705.08260, 2017.
- [57] R. Zhang, P. Isola, A. A. Efros, E. Shechtman, and O. Wang, "The unreasonable effectiveness of deep features as a perceptual metric," in *Proc. IEEE Conf. Comput. Vis. Pattern Recognit.*, pp. 586–595, 2018.
- [58] D. Eigen, C. Puhrsch, and R. Fergus, "Depth map prediction from a single image using a multi-scale deep network," *Adv. Neural Inf. Process. Syst.*, vol. 27, 2014.
- [59] A. Schmidt, O. Mohareri, S. DiMaio, M. C. Yip, and S. E. Salcudean, "Tracking and mapping in medical computer vision: A review," *Med. Image Anal.*, p. 103131, 2024.



surgical robotics, and deep learning.

SHAN LIN received the B.Sc. degree in electrical engineering from Xiamen University, Xiamen, China, in 2015, the M.S. degree in electrical engineering from Vanderbilt University, Nashville, TN, USA, in 2017, and the Ph.D. degree in electrical and computer engineering from the University of Washington, Seattle, WA, USA, in 2021. She is currently a Postdoctoral Researcher with the University of California, San Diego, La Jolla, CA, USA. Her research interests include robot vision,



JINGPEI LU received the B.Sc. and M.S. degrees in electrical engineering in 2018 and 2020, respectively, from the University of California San Diego, La Jolla, CA, USA, where he is currently working toward the Ph.D. degree in electrical engineering with the Department of Electrical and Computer Engineering. His research interests include computer vision and machine learning for robot perception and automation.



Disney Research, and Amazon Robotics. He received a B.Sc. from the University of Waterloo, an M.S. from the University of British Columbia, and a Ph.D. from Stanford University.

MICHAEL YIP is an Associate Professor at UC San Diego and directs the Advanced Robotics and Controls Laboratory. They focus on surgical robotics, 3D visual tracking and servoing, data-efficient machine learning for control and motion planning, and medical imaging. He has been nominated for and won several best paper awards at ICRA and IROS, the 2017 best paper award for RA-L, the NSF CAREER and the NIH Trailblazer award. Dr. Yip was previously with



SHREYA SAHA received her undergraduate degree in Computer Science and Engineering from National Institute of Technology, Durgapur in 2019 and her MS in Computer Science from University of California, San Diego in 2023. She is currently pursuing her PhD in Electrical and Computer Engineering from University of California, San Diego.



SAINAN LIU received a B.C.S. degree in computer science from the University of British Columbia, Vancouver, British Columbia, Canada, in 2016. She then obtained her M.S. and Ph.D. degrees in Computer Science and Engineering from the University of California San Diego, San Diego, California, U.S.A., in 2018 and 2022. Previously, she has held summer positions as a Research Associate Intern at Qualcomm, Multimedia, Computer Vision R&D, in 2017, an Applied Scientist Intern at Amazon, AWS Rekognition team, in 2018, a Research Scientist Intern at Waymo, Perception team, in 2019, a Research Scientist Intern at Intel AI Lab in 2020, and a Research Intern position at Google Research, Perception Team, in 2021. Since 2021, she has become a full-time A.I. Research Scientist at Intel Labs, San Diego, California, U.S.A.. Her research interests include 2D to 3D reconstruction, Virtual/Augmented Reality, 3D scene/video generation, and 2D/3D representation learning.



ZEKAI LIANG received his B.Sc. degree in Mechanical Design, Manufacturing, and Automation from Huazhong University of Science and Technology, Wuhan, China, in 2023. He's currently pursuing the M.Sc. degree in Electrical and Computer Engineering at the University of California, San Diego, La Jolla, CA, USA. His research interests include robot perception and visual learning.

...